Morphological regions and oblique incidence dot formation in a model of surface sputtering

Emmanuel O. Yewande,* Reiner Kree,† and Alexander K. Hartmann‡
Institut für Theoretische Physik, Universität Göttingen,
Friedrich-Hund Platz 1, 37077 Göttingen, Germany
(Dated: May 14, 2006)

We study solid surface morphology created by off-normal ion-beam sputtering with an atomistic, solid-on-solid model of sputter erosion. With respect to an earlier version of the model, we extend this model with the inclusion of lateral erosion. Using the 2-dimensional structure factor, we found an upper bound $\mu \simeq 2$, in the lateral straggle μ, for clear ripple formation. Above this upper bound, for longitudinal straggle $\sigma \gtrsim 1.7$, we found the possibility of dot formation (without sample rotation). Moreover, a temporal crossover from a hole topography to ripple topography with the same value of collision cascade parameters was found. Finally, a scaling analysis of the roughness, using the consecutive gradient approach, yields the growth exponents $\beta = 0.33$ and 0.67 for two different topographic regimes. The results are discussed in the context of the continuum theory.

PACS numbers: 05.10.-a,68.35.-p,79.20.-m

I. INTRODUCTION

Low energy bombardment of the surface of amorphous materials [1], semiconductors (amorphized by the sputtering processs) [2–4], and metallic materials (at low temperature) [5], by a beam of ions at off-normal incidence, often lead to ripple pattern formation. The ripple orientation is perpendicular to the projection of the ion beam direction, onto the surface plane, for small incidence angles, and parallel to the projection for grazing incidence. However, for a metallic surface with anisotropic diffusion, the orientation is perpendicular to a crystallographic direction (the one favored for diffusion) at small incidence angle [5].

According to the continuum theory [6–8], ripples arise, for all angles of incidence θ, from the curvature dependence of the sputter yield. The wavelength λ obtained within the continuum theory is given by $\lambda = 2\pi\sqrt{2K/|\nu|}$, where K is the surface diffusivity, and ν is a negative surface tension coefficient. Typical wavelengths are of the order of nanometers. In the absence of non-linearities, the θ dependent ν, being different along the parallel and perpendicular directions to ion projection, govern the ripple orientation. However, contrary to the predictions of the continuum theory (ccf. Figs. 12 and 15 of [8]), no ripples were observed in [9] for $\theta \lesssim 40^0$ under Xe ion irradiation of Si.

Other studies have shown that this influence of collision cascading on topography evolution extends to quantum dot formation at $\theta = 0$ on non-rotated substrates[10], and at $\theta > 0$ on rotated substrates [11, 12]. Also, the influence of collision cascade statistics on grazing incidence sputtering of cristal surfaces has recently been studied [13] and deviations from the Gaussian distribution [14] which has been the basis of the theoretical models so far in use [6, 7, 15] have been observed. But till now the ripple phase boundaries arising from such influence are thought to be time (i.e. fluence) independent. Furthermore, up till now, dependence of ripple formation on the lateral straggle μ, though acknowledged, is often ignored on accounts of isotropic or symmetric cascading for simplicity.

An atomistic MC model of sputter-erosion, introduced in Ref. [15], captures the universal features of material-surface modification by ion beam treatment [16, 17], and affords a way of exploring the different phases in the surface morphology. In this paper, we extend this model with inclusion of lateral erosion. This includes stronger non-linearities in the sputtering process. Hence, the exponential-growth tendency of the ripple amplitude occuring within the linear theory is more stabilized [18, 19]. Furthermore, we show that the angle θ_r, above which ripple formation occur, depends on the longitudinal straggle σ of the ion beam, with higher σ resulting in lower θ_r.

Moreover, we find that there are two distinct creation mechanism for ripple: In one region of the parameter space, there is a transition from hole topography at an early time, to ripple topography at a later time. For other parameters, the ripples are created from a simple rough topography at early times. Our results also indicate the crucial role of the value of μ for ripple formation. If we chose μ larger enough, then, without sample rotation (and $\theta > 0$), we find dots/nano-sized islands similar to those observed in the experiments [20, 21], and theory [10]. Our results suggest that by using new projectile/target combinations one might find yet unobserved surface topographies. We mention below some promising projectile/target combinations which might serve as guidelines for experimentalists.

In the next section, we describe our simulation model.

*Electronic address: yewande@theorie.physik.uni-goettingen.de
†Electronic address: kree@theorie.physik.uni-goettingen.de
‡Electronic address: hartmann@theorie.physik.uni-goettingen.de

In the main part we present and discuss our results.

II. NUMERICAL SIMULATION METHODS

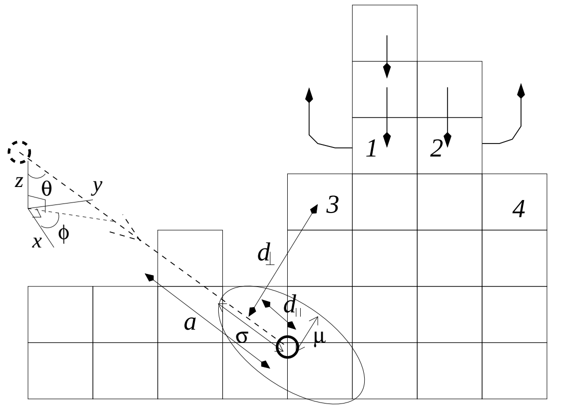

FIG. 1: Sketch showing lateral erosion of surface atoms, and collision cascade ellipsoid, as described in the text. Erosion of atom at position 1 or 2 triggers a relaxation, which ensures there is no overhang; the atom at position 3 or 4 is only eroded, without surface relaxation.

We study system sizes $L \times L$ with periodic boundary conditions. The material surface is defined by a time-dependent discrete height function $h(x, y, t)$ [$(2 + 1)D$ solid-on-solid (SOS) model] which is initially flat, i.e, $h(x, y, 0)$ =constant. We have included surface roughening via sputtering and surface smoothening via surface diffusion. Each simulation step consist of the sputtering generated by one ion and a certain number of diffusion steps. The simulation time is measured in terms of these steps and corresponds to the fluence in experiments. For details see Ref. [16]. Here we only display the main ingredients of the methods, for the convenience of the reader, and describe the extensions with respect to the original method.

We simulate the sputtering process as a combination of ion motion and erosion of atoms. The ion source, at some random position in a plane directly above the surface plane, projects the ions along a trajectory inclined at θ to the vertical and with azimuth ϕ. After penetrating the solid through a depth a, measured along the ion trajectory, each ion comes to rest and distributes its kinetic energy ε. Erosion of surface atoms occur with a probability, which is proportional to the energy imparted to them by the impinging ion. The distribution of the kinetic energy of an impinging ion is approximated [14] by the Gaussian

$$E(\mathbf{r}) = \frac{\varepsilon}{\sqrt{8\pi^3}\sigma\mu^2} \exp\left\{-\frac{d_\parallel^2}{2\sigma^2} - \frac{d_\perp^2}{2\mu^2}\right\}, \qquad (1)$$

where $d_\parallel = z + a$ is the distance of the surface atom, from the final stopping point of the ion, along the ion trajectory. $d_\perp$ is the distance of the surface atom perpendicular to the ion trajectory. Hence, we use the local coordinate system of the ion with origin at the point of penetration, and the z-axis coinciding with the ion trajectory [15, 16]. A sketch is provided in Fig. 1. Note that all parameters depend on the experimental parameters like materials, ion energy and angle of incidence. They can be estimated using the SRIM simulation package [22] (see the next section). Except where otherwise stated, $a = 6.0$, $\theta = 50.0^0$, $\phi = 22.0^0$, and ϵ is chosen to be $(2\pi)^{3/2}\sigma\mu^2$. Here, in contrast to previous studies, we vary systematically the values of μ and σ mimicing different material combinations.

Furthermore, we extend the sputtering model by considering lateral erosion of surface atoms; thus including non-linearity in a manner analogous to the Kardar-Parisi-Zhang (KPZ) non-linearity, that arises from lateral attachment of adatoms in surface growth [23]. This has the effect of relaxing the surface [24] (expecially as local surface slopes increase, since $h(i) \to h(i) - n_i$ where n_i is the number of surface atoms eroded in column i at that instant, due to their being closer to the stopping point of ion than topmost atom in column (see Fig. 1).

Surface migration is simulated [16, 25] as a nearest neighbor Monte Carlo hopping process, with a site i and nearest neighbor site j chosen randomly; and a hop $i \to j$ allowed with probability

$$p_{i \to j} \propto \exp\left(-\frac{E}{k_B T}\right), \qquad (2)$$

where $E = E_S + nnE_{NN} + E_{SB}$ is an energy barrier to hopping, comprising of a substrate term $E_S = 0.75$eV, a nearest neighbor term $E_{NN} = 0.18$eV and a step barrier term E_{SB}; nn is the number of in-plane nearest neighbors of the diffusing atom; T is the substrate temperature; and k_B is the Boltzmann's constant. $E_{SB} = 0.15$eV if there is no vacant next-nearest neighbors in the plane below the hopping atom (at site i), and there is *at least* a vacant next-nearest neighbor in the plane below the hopped atom (at site j); otherwise $E_{SB} = 0$. Thus this model discourages diffusion to a down-step edge but once the approach is made, it does not discourage a hop down the step (i.e since $E_{SB} = 0$ then; see Fig. 1 of [25]).

A local heating of the surface occurs right after ion impact, followed by rapid cooling; hence surface diffusion is greatly enhanced, due to higher effective temperatures arising from the ion impacts. Consequently, we have used a higher effective temperature $k_B T = 0.1$eV in our simulations, which was estimated in our previous work [16], based on a calculation of the spatio-temporal development of the temperature, arising from the local heating [26] (see also [27]).

III. RESULTS AND DISCUSSION

We have used system sizes $L^2 = 128^2$. Distances are in units of a lattice constant, and time in ions/atom. By varying the collision cascade parameters σ and μ, we explore the full topographic features of this sputter-erosion model, for typical ion energies on the order of 1keV; keeping a and θ constant.

We have studied about 50 different (σ, μ) combinations. We observed six different types of the qualitative behavior, corresponding to six different regions in the (σ, μ) space. In Fig. 2 these six regions are indicated for $t = 3$ ions/surface atom at which almost all the surface topographic features are distinct; the corresponding profiles are shown in Fig 3. The boundaries shown in this sketch do not represent abrupt transitions from one topography to another, as we shall see below (in Figs. 11, 10). Rather we observe often a smooth crossover from one behavior to the other. For this reason, we have not used straight lines to represent them in the diagram. Also, we have focussed on a typical time $t = 3$, corresponding to timescales often used in experiments, which exhibit a rich behavior as a function of the straggling parameters μ and σ. Only one systematic change of the boundaries occurs with time, which is described below. Finally, although the sketch is specifically at $\theta = 50^0$, similar "phases" also occur at other values of θ, with slight deviations at the boundaries.

We performed SRIM simulations [22] to estimate the following experimental parameters, that might yield parameter combinations shown in the figure (2). Please note that the following list is just to give a few examples. Region V: $1.5 - 1.7keV$ neon(Ne)-ion sputtering of copper(Cu); $1.2 - 1.4keV$ Ne-ion sputtering of germanium(Ge). Region IV: $650 - 800eV$ Ne-ion sputtering of silicon(Si). Region III: $800eV - 1.1keV$ Ar-ion sputtering of silicon(Si); $550 - 700eV$ Ne-ion sputtering of C. With fluences of the order of $\sim 10^{14} - \sim 10^{15}$ ions/cm^2. Note that for most materials and parameter combinations $\sigma \leq \mu$, hence the region VI might be difficult to access.

Also, SRIM simulations reveal that very large σ and μ, i.e, beyond the values considered here, are impractical, since they can only occur for a higher a. Whereas, the value of a is itself restricted by the range of ion energies that lead to ripple formation. We are not aware of an experimental study of the sputtering behavior where the parameters are varied systematically in the μ-σ plane. Hence, when using these parameters in experiments, one might be able to observe new surface topographies.

A brief description of each topographic region in Fig. 3, including the behavior at later times $t \geq 3$ (ions/surface atom), is as follows:

Region I: rough surface [see Fig. 3(I)] which, as time increases, evolves to a hole topography. The *sizes* of the holes grow and finally coalesce to a ripple topography at long times (Fig. 4).

Region II: holes are already prominent in this region [see Fig. 3(II)]; here the *number* of holes increase with time, and again ripples are formed at long times, but at an earlier time than as in region I (not shown as separate figure).

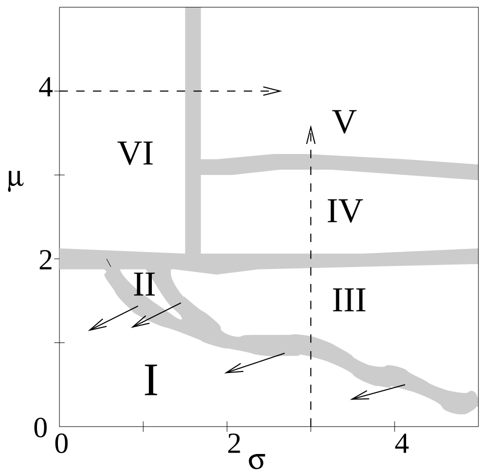

FIG. 2: Different topographic regions ($\theta = 50^0$, $a = 6$). Region I: rough surface; II: holes; III: clear ripples oriented perpendicular to ion beam direction; IV: short ripples (resulting from increased mu); V: dots; VI: non-oriented structures. The short arrows indicate the evoltuion of the boundaries between different regions with respect to time. Hence, region III grows at the expense of region I, while region II describes only a short transient. The long dashed arrows indicate the directions referred to in Fig. 8. The units are for easier reference in the discussion.

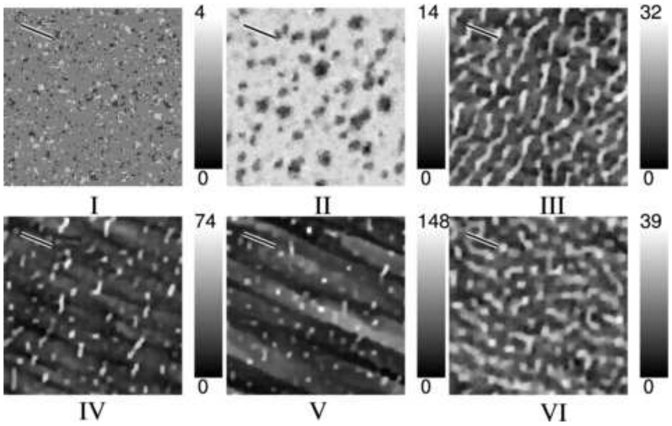

FIG. 3: Profiles for parameters chosen from each topographic region in Fig. 2; $\theta = 50^0$, $a = 6$, $t = 3.0$. (I) $\sigma = 1$, $\mu = 0.5$; (II) $\sigma = 1$, $\mu = 1.5$; (III) $\sigma = 3$, $\mu = 1.5$; (IV) $\sigma = 4$, $\mu = 2.5$; (V) $\sigma = 5$, $\mu = 5$; (VI) $\sigma = 0.5$, $\mu = 5$. The bar, on all profiles, denote the ion beam direction

The number of holes decrease when increasing the sputtering depth a [Fig. 5 (a)-(c)]. On the other hand, if we vary θ, the number of holes increase with increasing θ [Fig. 5 (d)-(f)]. Ripples can be formed here at this time (t=3) if θ is increased beyond $\theta_r(t = 3) \simeq 60^0$.

Region III: the ripple phase [15, 16]. Having observed in regions I and II that holes evolve into ripples with time, we studied this region from the very earliest times (t=0-3) but found only very tiny holes, i.e not as pronounced

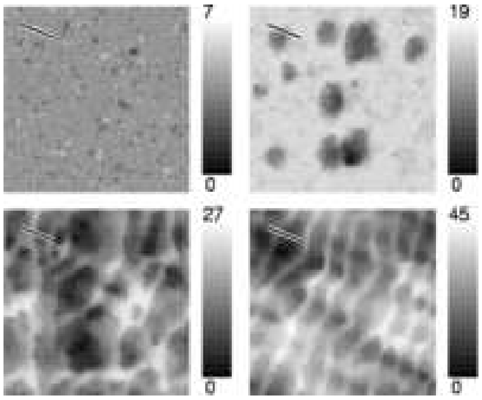

FIG. 4: Surface profiles of region I, $\sigma = 1$, $\mu = 1$. From top-bottom, left-right, $t = 3$, 20, 40, and 90.

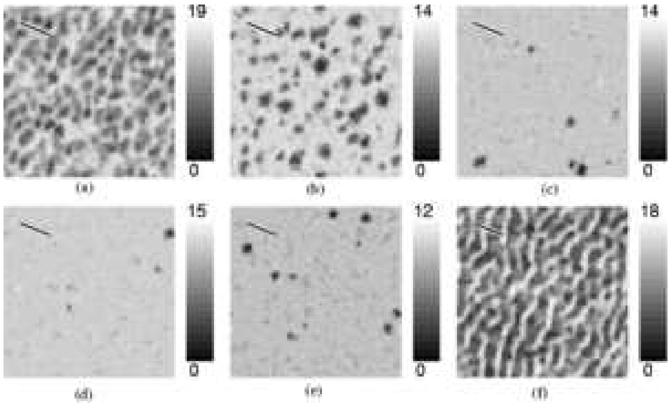

FIG. 5: Surface profiles of region II, t=3 ions/atom ($\sigma = 1$, $\mu = 1.5$). Top row; $\theta = 50^0$, (a) $a = 5$, (b) $a = 6$, and (c) $a = 7$. Bottom row; $a = 6$, (d) $\theta = 40^0$, (e) 45^0, and (f) 60^0.

as in region II, in the course of ripple formation (see Fig. 6). $\theta_r \simeq 30^0$ in this region. Thus, comparing regions I,II and III, there seem to be two different processes of ripple formation. Ripples can be formed quickly by evolving directly from a slightly rough surface, or they can be formed slowly via the creation of holes, which coalesce to ripples on longer time scales. Note that in regions I and II, the resulting ripple wavelength is smaller than the size of the holes generated on smaller time, while in region III the ripple wavelength is larger than the tiny holes.

To summarize the dynamical behavior observed in regions I-III, for long (but not infinite) times ripples are formed everywhere, but region III grows on the expense of the two other regions. Region II represents only a short transient behavior. It might extent further to larger values of σ in a very narrow range between region I and III, but we cannot resolve this with our limited number of parameter combinations. Please note that at very long times, beyond the usual time scales accessible in standard experiments, nonlinear effects become more important and the ripples coarsen and disappear again [15, 16].

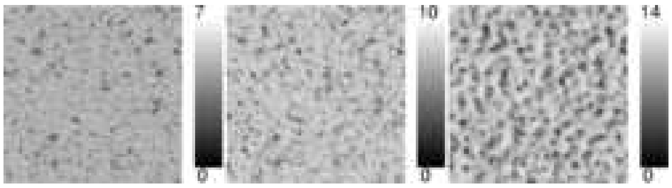

FIG. 6: Surface profiles of region III, at very early times. From left-right, t=0.1, 0.2 and 0.5 ions/atom ($\sigma = 3$, $\mu = 1.5$, $\theta = 50^0$, $a = 6$).

We also studied here the case of smaller angles, e.g. $\theta = 30°$, see Fig. 7. Hence, for lower angles of incidence, ripple formation is shifted to later times, but the ripple tendency again increases when increasing the longitudinal struggle σ. This indicates that there might be a lower critical angle θ_c, below which no ripple formation happens even at long times. Such an effect has been observed in experiments [9] of sputtering Xe^+ on Si, where below $\theta_C = 40°$ no ripples have been found at finite but long ion fluences. For even smaller angles like $\theta = 20°$, we indeed do not observe ripple formation within the time scales (i.e. fluences) we can reach in our simulations. Note that a general statement about the existence of such a critical angle $\theta_c(\mu, \sigma)$ would require simulations up to very large times for all parameters studied here, which is beyond the numerical capacities. Hence, we remain with the statement that our numerical results indicate that such critical angles indeed exist, without the possibility to determine them precisely.

It was shown in Ref. [15], that the ripples in this region rotate by 90^0 with increasing fluence (see also [28]).

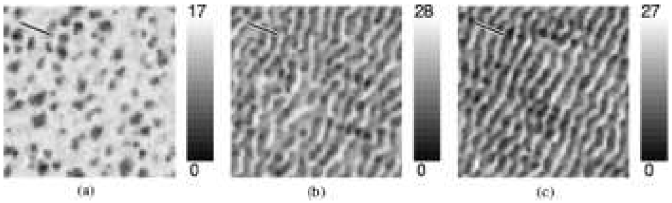

FIG. 7: $\theta = 30^0$, $a = 6$, $\mu = 1.5$; $\sigma = 2$ (a); $\sigma = 3$ (b); and $\sigma = 5$ (c).

Region IV: consists of a mixture of dots and short ripples, which eventually give way to the dot “phase” (region V), as σ is increased. Hence, this region seems to “interpolate” between regions III and V.

Region V: consists of dots. These dots are formed on some ripple-like structures oriented perpendicular to the ion beam direction, as discussed below in more detail. Noting that our model is a solid on solid model on a square lattice, the dots are not unsimilar to the QDs predicted by theory [10, 12] and observed in experiments [21, 29].

Region VI: consists of non-oriented structures exhibiting a typical lengthscale, but only a slight orientational preference parallel to the ion beam. This region, as mentioned above, is probably difficult to access in experiments.

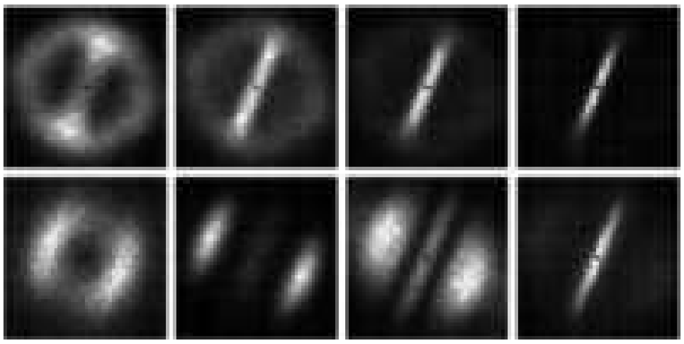

FIG. 8: $2D$ structure factor (L=128). Top, along $\mu = 4$ in Fig. 2, left-right: $\sigma = 0.5$, 1.0, 1.5, and 3.0. Bottom, along $\sigma = 3$, left-right: $\mu = 0.5$, 1.0, 1.5, and 3.0

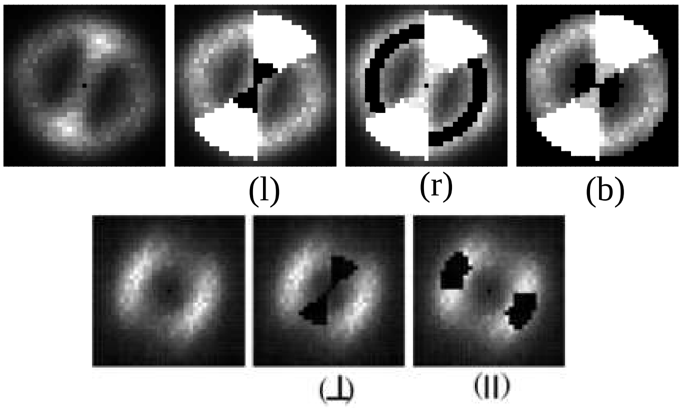

FIG. 9: Separation of the $2D$ S(k) (first image top and bottom) into regions (in black from second image), for the purpose of our analysis. The letters l, r, b, denote line, ring and background, respectively; and the symbols, $\perp$ and $\|$, denote the perpendicular and parallel directions, respectively; as referred to in the text. The white regions are excluded from the analysis.

A closer look at the dot profiles of region V in Fig. 3 reveals the presence of some underlying large-scale structures. We now discuss this region and its adjacent regions III and V with more detail. The underlying structure is clearly seen in a $2D$ structure factor, $S(\mathbf{k}) = \langle h(\mathbf{k})h(-\mathbf{k})\rangle$, where h($\mathbf{k}$), the fourier transform of the height profile $h(\mathbf{r})$, with mean $\langle h\rangle = \sum_{\mathbf{r}} h(\mathbf{r})/L^2$, at time t, is given by

$$h(\mathbf{k}) = \frac{1}{L}\sum_{\mathbf{r}}[h(\mathbf{r}) - \langle h\rangle]\exp(i\mathbf{k}\cdot\mathbf{r}). \qquad (3)$$

The $2D$ structure factor shown in Fig. 8 has been obtained from an average of 600 independent runs, for parameter along $\mu = 4$ (top row), and along $\sigma = 3.0$ (bottom row). In these diagrams the structure factor for the k-vector $(k_x, k_y) = (0, 0)$ is displayed in the center and the corners represent the values for $(k_x, k_y) = 2\pi(\pm 1/8, \pm 1/8)$. The case of $\mu = 4.0$, when moving from small values of σ to larger values (i.e. left-right in Fig. 2) is shown in the top row of Fig. 8. For small values of σ, we are in region VI, where we see a typical wavelength, but almost no orientation. This translates to a ring visible in the $S(\mathbf{k})$ plot. Note that there is a slight preference for an orientation parallel to the ion beam, being visible via two peaks in $S(\mathbf{k})$ at wave vectors perpendicular to the ion beam (see also the real-space profile, of region VI, in Fig. 3). When increasing σ, one moves into region V. Here a line perpendicular to the ion beam emerges in the structure factor rather abruptly around $\mu = 1$. This line represents the underlying 1D structures parallel to the ion beam, being visible in Fig. 3. Note that the "dots" emerge on top of these structures; in the $2D$ structure factor their signal is too weak to be visible.

On the other hand, along $\sigma = 3.0$, we initially see (bottom row of Fig. 8) an orientation, spread around ion beam direction (for instance, at $\mu = 1.0$), with a more restricted range of k which is typical of the thin wobbly ripples. As μ increases, we move to the region V as discussed above, but we do not observe an abrupt change, because for a large range of values of μ, ripples, dots and the underlying structures with parallel orientation, to ion beam direction, coexist (see below).

To study the crossover or transition from one region to the other in a quantitative way, it might be more instructive to look at order parameters which are numbers rather than the full $2D$ structure factor. We first define a quantity $Q = S^m(\mathbf{k}_\perp)/S^m(\mathbf{k}_\|)$, where $S^m(\mathbf{k}_{\|(\perp)})$ is the maximum, for $\mathbf{k}$ parallel (perpendicular) to ion beam direction. This quantity detects the change of orientational order.

When moving along $\mu = 4$ from region VI into region V we expect a rather abrupt change of the behavior from the visual inspection of the $2D$ structure factor (top row of 8). The behavior of Q when changing σ for $\mu = 4$ is displayed in the inset of Fig. 10. For small values of σ, i.e. in region VI, there is only a slight preference of structures parallel to the ion beam (corresponding to $\mathbf{k}_\perp$) which leads to small values $Q \approx 2$. When going beyond $\sigma = 1$, i.e. when moving into region V, the domination of the longitudinal structures increase, leading to a growth of Q.

We, furthermore, want to go beyond studying the height of peaks of $S(k)$ by examining the presence or absence of a typical length scale in the system. This length scale is visible in the $2D$ structure factor via bright spots (oriented) or a bright ring. For this purpose, we also look at the relative weights

$$q_{x/y} = \frac{\int_{A_x} S(\mathbf{k})d\mathbf{a}}{\int_{A_y} S(\mathbf{k})d\mathbf{a}}, \qquad (4)$$

of certain areas in the $2D$ structure factor, where the integration $d\mathbf{a}$ extends over areas A_x/A_y of $\mathbf{k}$-points. The indices $x, y = l, r, b$, refer to $\mathbf{k}$ values on the line, ring and background (outside line and ring) respectively, as shown in the upper part of Fig. 9. The white regions, in this figure, are excluded from our analysis, because they contain a superposition of $\mathbf{k}$s on both the line, and the ring. A plot for $q_{r/b}$ is shown in Fig. 10, other combinations (not shown) yield results with information not going beyond the study of Q. For $q_{r/b}$ we observe an abrupt change around $\sigma = 1$ with the ring becoming almost indistinguishable ($q_{r/b} \approx 1$) from the background for $\sigma > 1 - 1.5$, signaling the disappearance of a typical length scale around $\sigma = 1$. Note that $q_{r/b}$ stays almost constant for the full region V, in contrast to the behavior of Q.

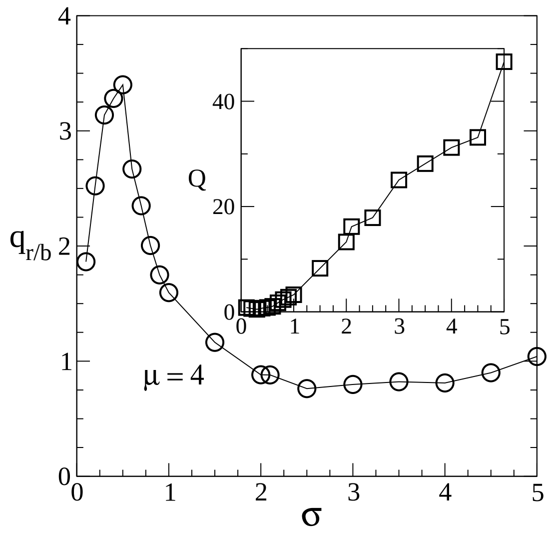

FIG. 10: Plot of the quantities $q_{r/b}$ and Q (inset) as a function of σ, along $\mu = 4.0$, as described in the text. Lines are guides to the eyes only.

Now, we turn to the behavior along the $\sigma = 3$ line, i.e. when moving from region I, into region III, then IV and finally V. The behavior of Q as function of μ (bottom row of Fig. 8) is displayed in the inset of Fig. 11. The crossover around $\mu \simeq 2$ from the ripple region (II) where $k_\parallel$ wave vectors dominate ($Q < 1$) to the region V where $k_\perp$-structures dominate is clearly visible.

The same result is obtained, when again studying not only peaks, but integrated structure factors over certain selected areas. Hence, we also study k-vectors parallel and perpendicular to the ion beam ($x, y = \parallel, \perp$), as shown in the lower part of Fig. 9. Also $q_{\perp/\parallel}$ exhibits a strong growth for $\mu > 2$, i.e. when moving into region III.

Finally, a study of $q_{r/b}$ (not shown) again confirms the the loss of a certain length scale when moving into region V. This is again visible via the disappearance of weight on the ring in the $2D$ structure factor with respect to the background [see again Fig. 8]. In any case, we have mainly looked at snapshots at time $t = 3$, corresponding to typical experimental fluences of 10^{15} ions/cm^2 (as already stated above). Hence, the location of the exact

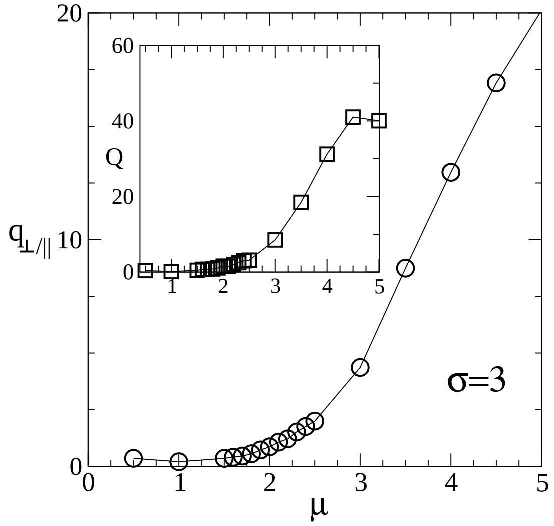

FIG. 11: Plot of the quantities $q_{\perp/\parallel}$ and Q (inset) as a function of μ, along $\sigma = 3.0$, as described in the text. Lines are guides to the eyes only.

boundaries between the different regions, is not a major interest here. We only want to demonstrate, that indeed order-parameter-like functions can be defined. The full information is contained in the $2D$ structure factors.

Next, we consider the predictions of the continuum theory, as pertains to this study. In the asymptotic limit, the morphology of sputtered surfaces may be described by the noisy Kuramoto Sivashinsky equation [7]

$$\partial_t h = \nu_\parallel \partial_x^2 h + \nu_\perp \partial_y^2 h + \frac{\lambda_\parallel}{2}(\partial_x h)^2 + \frac{\lambda_\perp}{2}(\partial_y h)^2 - K\partial^4 h + \eta, \tag{5}$$

where $\nu_\parallel(\nu_\perp)$, $\lambda_\parallel(\lambda_\perp)$, is the effective surface tension coefficient, and nonlinear coefficient, respectively, along a direction parallel (perpendicular) to the projection of the ion beam direction onto the surface plane (here, the x-axis is parallel to the projection); K is the surface diffusion constant; and η is an uncorrelated noise term, with zero mean. These coefficients are explicitly given, in terms of the sputtering parameters, in ref. [8]. Note that erosion of surface material tends to maximize the exposed area, so-called negative surface tension, hence, for the sputtering phenomena, this instability constrains the coefficients $\nu_\parallel$ and $\nu_\perp$ to be negative.

At early times, the local slopes are small enough in most of the regions for us to ignore the nonlinearities; we are therefore left with a noisy Bradley-Harper equation [6]. A plot of the coefficients ν for our parameter range, along $\sigma = 3$, is shown in Fig. 12; $|\nu_\parallel|$ and $|\nu_\perp|$ are nonzero almost always, which implies the presence of two length-scales. Hence, according to the linear continuum theory, ripples parallel and perpendicular to the ion beam direction are always present in the system; the one observed is the one for which $|\nu|$ is highest; i.e, with the highest amplitude-growth rate $R = -(\nu_\parallel k_\parallel^2 + \nu_\perp k_\perp^2) - K(k_\parallel^2 + k_\perp^2)^2$

[6].

We now try to understand roughly the behavior along the above discussed $\sigma = 3$ and $\mu = 4$ lines within the linear theory. In Fig. 12 the values of $\nu_{\parallel}$ and $\nu_{\perp}$ are shown as function of μ (main plot) and σ (inset) along these lines. For the case $\mu = 4$ (see inset), we observe that $\nu_{\parallel} > 0$ for all values of σ, hence the preferential orientation is always parallel to the ion beam, as observed. To understand the crossover from region VI to region V, maybe one has to consider nonlinear terms. For the $\sigma = 3$ line, we observe $|\nu_{\perp}| \approx |\nu_{\parallel}|$ for $\mu < 1$, which is compatible with the behavior in region I, where no preferential orientation is observed. For $1 \lesssim \mu \lesssim 2.5$, $|\nu_{\parallel}| > |\nu_{\perp}|$ which implies the dominance of ripples with $k_{\parallel}$ (i.e, with wavelength $\lambda = 2\pi\sqrt{2K/|\nu_{\parallel}|}$), as we have seen in region III and partly in the crossover region IV. In region IV ripples are still present, but dominate less.

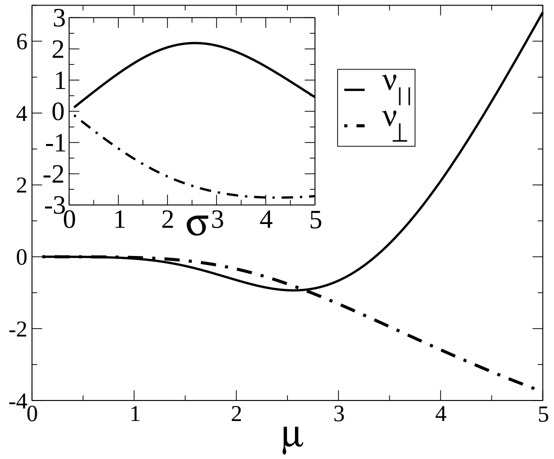

FIG. 12: The surface tension coefficients of Eq. 5, along $\sigma = 3.0$, for our simulation parameters. $\theta = 50°$, $a = 6.0$

For μ above this range, the structures with $k_{\perp}$ dominate. However, the positive value of $\nu_{\parallel}$ for higher μ is contrary to our results, since it implies a preferential smoothening along the parallel direction. We have not observed such smoothening, here probably nonlinear effects are more important. If we consider the maximum of $|\nu_{\parallel}|$ and $|\nu_{\perp}|$ for the region where $\nu_{\parallel} < 0$ and/or $\nu_{\perp} < 0$, then we see that this maximum is obtained in region V for large μ. Since larger $|\nu|$ implies a higher tendency to maximize the exposed surface area, i.e. increased roughening, one should expect rougher surfaces in region V. Indeed we observe that region V is rougher than e.g. region III, as we shall see below.

But, before we proceed, we should recall that regions I and II eventually evolve to a similar ripple topography as in region III; region IV is an intermediate stage; and VI is hardly experimentally accessible. Therefore, we are interested in two different scaling regions, i.e, arising from ripple-yielding, as well as dot yielding parameters. We use the finite-size scaling behavior of the surface

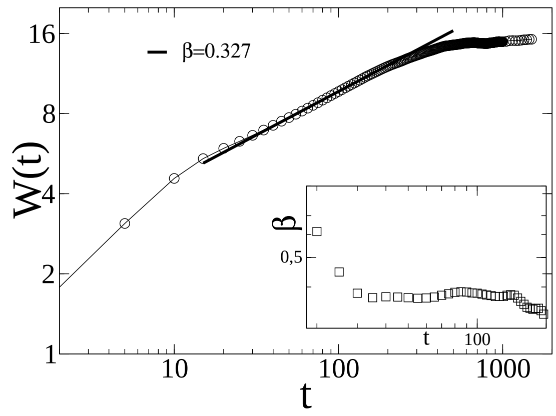

FIG. 13: Surface width W versus time, $\sigma = 3$, $\mu = 1.5$ (region III), $\theta = 50^0$. In the inset is a plot of the consecutive βs for $t = 20 - 200$, where the lower and upper cutoffs are seen to occur at $t = 35$ and 150 respectively.

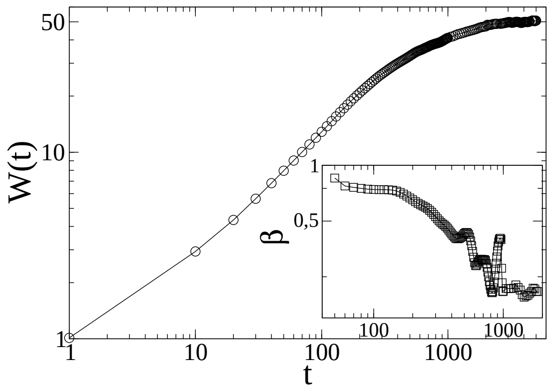

FIG. 14: Surface width W versus time, $\sigma = 5$, $\mu = 5$ (region V), $\theta = 50^0$. In the inset, time is in multiples of 10^2; there are two scaling regions $t = 40 - 140$ and $t = 1000 - 1800$, which yields $\beta = 0.665$ and 0.137 respectively.

width/roughness,

$$W(L,t) = L^{\alpha} f(\frac{t}{L^z}), \tag{6}$$

where α and β are the roughness exponent and growth exponent, respectively; and $W = \sum_{\mathbf{r}}(h(\mathbf{r}) - \langle h \rangle)^2/L^2$, i.e, W is the root-mean-squared fluctuations in the surface height. (6) defines two scaling regions, separated at the saturation time $t_s(L) \propto L^z$. $z = \alpha/\beta$ is the dynamic exponent. In the first region ($t << L^z$), $W \propto t^{\beta}$, independent of L; and in the second region ($t >> L^z$), $W \propto L^{\alpha}$, i.e., constant in time [30]. A scaling argument in [19] reveals that t_s increases with the diffusion coefficient, and with decreasing strength of non-linearities [31].

In the following roughness analysis, we rescale the time unit such that L^2 particles are eroded in unit time, which is analogous to the measure of time in simulations of epitaxial growth on vicinal surfaces. We obtained our scaling exponents from an average of 600 independent runs.

Fig. 13 is a plot of the surface width $W(t)$ for $L = 128$, we determine the actual scaling region of β from the consecutive slopes [30] of W(t) for $t < L^z$; shown in the inset of Figs. 13 and 14 where a fit to this region gives $\beta = 0.327 \pm 0.001$ and $\beta = 0.665 \pm 0.003$ for the topographic regions (see Fig. 2) III and V respectively; i.e., the long-time scaling behavior for sputtering conditions coinciding with the respective regions.

Our exponents are quite different from the scaling of the KPZ equation [23] in (2+1) dimensions [30, 32], which shows that for these parameter choices, either one or both of the negative surface tension coefficients, in the noisy KS equation [7], do not renormalize to positive values. That is, if indeed, this atomistic model which is known to accurately describe the morphology of sputtered surfaces at early and long times [15–17], can be represented by the noisy KS equation, in the asymptotic limit, as expected for the sputtering phenomenon.

IV. CONCLUSIONS

We have extended the study of surface topography induced by ion bombardment beyond the circular-symmetric collision cascade case $\sigma = \mu = 1$; using a discrete atomistic Monte Carlo model. We found a strong influence of the lateral straggle μ on the surface morphology. Below an upper bound $\mu \simeq 2$, clear ripple formation is possible. Depending on the longitudinal straggle σ, ripples appear on different time scales, and through two different creation mechanisms, equivalent to a growth of the ripple forming parameter region on the expense of the hole region. These ripples persist on intermediate time scales, but disappear again, as found in previous studies for one parameter combination, on longer times scales. Above the upper bound $\mu \simeq 2$ nanosized islands were found for longitudinal straggle $\sigma \gtrsim 1.7$. These structures appear from our studies to be stable on longer time scales. Also, we found the possibility of different incidence θ_r, above which ripple formation is possible, as in the experiment; our results indicating that high value of the longitudinal straggling result in lower value of θ_r.

Comparison of our results with the continuum theory, reveal that dot formation is the result of the interplay between two (ripple-like) structures of perpendicular orientation: i.e, structures with wave vector either parallel or perpendicular to the ion beam direction. The tendency, due to the low incidence angle, is for the ripples with wave vector parallel to the ion beam direction to dominate. However, at high perpendicular straggle, ripple-like structures with wave vector perpendicular dominate by pinching off (or shortening), the ripples with wave vector parallel, into dots. This would seem to suggest a possible structural difference between dots formed from off-normal incidence sputtering, where there is a broken symmetry as a result of tilting the ion beam to the surface normal, and dots formed from normal incidence sputtering, where there is no such broken symmetry.

We found that the scaling of the fluctuations in the surface height depends on the collision cascade parameters; whereby the roughness becomes saturated much earlier in the ripple region than in the dot region. Our results indicate the possibility of yet unobserved surface topographies. In future experiments, a systematic study covering the full parameter space (at least in the range ($\sigma \leq \mu$) would be very interesting. So far, to our knowledge, this has not been done. Furthermore, it would be nice to investigate the small-time behavior, i.e. the ripple formation process, experimentally. In this way one could verify whether the two different creation mechanisms we have observed, hole-coalescence and creation from a rough surface, can be observed in experimental systems.

Finally, it would be nice to include smoothening in the sputtering behavior, along the lines of Ref. [33]. This has been discussed in the continuum theory [34], as effective surface relaxation. We have not implemented it explicitly in the sputtering mechanism, because it is implicit in our surface diffusion mechanism, manifested in the higher effective temperature due to local heating (i.e, in thermal spikes) of the surface at the impact point.

Acknowledgments

We have profited much from fruitful discussions with K.P. Lieb, H. Hofsss, M. Uhrmacher and C. Ronning. We thank B. Burghardt for critically reading the manuscript. This work was funded by the DFG (*Deutsche Forschungsgemeinschaft*) within the SFB (*Sonderforschungbereich*) 602: *Complex Structures in Condensed Matter from Atomic to Mesoscopic Scales* and by the *VolkswagenStiftung* (Germany) within the program "Nachwuchsgruppen an Universitäten".

[1] T. M. Mayer, E. Chason, and A. J. Howard, J. Appl. Phys. **76**, 1633 (1994).
[2] E. Chason, T. M. Mayer, B. K. Kellerman, D. T. McIlroy, and A. J. Howard, Phys. Rev. Lett. **72**, 3040 (1994).
[3] J. Erlebacher, M. J. Aziz, E. Chason, M. B. Sinclair, and J. A. Floro, Phys. Rev. Lett **82**, 2330 (1999).
[4] S. Habenicht, K. P. Lieb, J. Koch, and A. D. Wieck, Phys. Rev. B **65**, 115327 (2002).
[5] S. Rusponi, G. Costantini, C. Boragno, and U. Valbusa, Phys. Rev. Lett. **81**, 2735 (1998).
[6] R. M. Bradley and J. M. E. Harper, J. Vac. Sci. Technol. A **6**, 2390, (1988); and references therein.
[7] R. Cuerno and A. -L. Barabási, Phys. Rev. Lett. **74**, 4746 (1995).
[8] M. Makeev, R. Cuerno and A. -L. Barabási, Nuc. Instr. and Meth. in Phys. Res. B **197**, 185 (2002).

[9] G. Carter, and V. Vishnyakov, Phys. Rev. B **54**, 17647 (1996).
[10] B. Kahng, H. Jeong, and A.-L. Barabási, Appl. Phys. Lett. **78**, 805 (2001).
[11] R. Mark Bradley, Phys. Rev. E **54**, 6149 (1996).
[12] F. Frost, Appl. Phys. A **74**, 131 (2002).
[13] M. Feix, A. Hartmann, R. Kree, J. Muñoz-García, and R. Cuerno, Phys. Rev. B 71, 125407 (2005).
[14] P. Sigmund, Phys. Rev. **184**, 383 (1969).
[15] A. K. Hartmann, R. Kree, U. Geyer, and M. Kölbel, Phys. Rev. B **65**, 193403 (2002).
[16] E. O. Yewande, A. K. Hartmann, and R. Kree, Phys. Rev. B **71**, 195405 (2005).
[17] A.-D. Brown, J. Erlebacher, W.-L. Chan, and E. Chason, Phys. Rev. Lett. **95**, 056101 (2005).
[18] M. Rost and J. Krug, Phys. Rev. Lett. **75**, 3894 (1995).
[19] S. Park, B. Kahng, H. Jeong, and A.-L. Barabási, Phys. Rev. Lett. **83**, 3486 (1999).
[20] F. Frost, A. Schindler, and F. Bigl, Phys. Rev Lett **85**, 4116 (2000).
[21] S. Facsko, T. Dekorsy, C. Koerdt, C. Trappe, H. Kurz, A. Vogt, and H. L. Hartnagel, Science **285**, 1551 (1999).
[22] J.F. Ziegler, J.P. Biersack and K. Littmark, *The Stopping and Range of Ions in Matter*, (Pergamon, New York 1985); see also `http://www.srim.org/`.
[23] M. Kardar, G. Parisi, and Y.-C. Zhang, Phys. Rev. Lett. **56**, 889 (1986).
[24] E. O. Yewande, unpublished.
[25] P. Šmilauer, M. R. Wilby, and D. D. Vvedensky, Phys. Rev. B **47**, 4119 (1993).
[26] N.A. Marks, Phys. Rev. B **56**, 2441 (1997)
[27] J. Melngailis, J. Vac. Sci. Technol. B **5**, 469 (1987).
[28] A.-D. Brown and J. Erlebacher, Phys. Rev. B **72**, 075350 (2005).
[29] R. Gago, L. Vázquez, R. Cuerno, M. Varela, C. Ballesteros, and J. M. Albella, Appl. Phys. Lett. **78**, 3316 (2001).
[30] A. -L. Barabási and H. E. Stanley, *Fractal Concepts in Surface Growth* (Cambridge University Press, Cambridge, 1995).
[31] See also: Z.-W. Lai and S. Das Sarma, Phys. Rev. Lett. **66**, 2348 (1991); where another non-linearity, distinct from the KPZ non-linearity was shown to affect the surface topography, in conserved MBE, in a similar manner.
[32] J. G. Amar and F. Family, Phys. Rev. A **41**, 3399 (1990).
[33] P. Bedrossian, J. E. Houston, J. Y. Tsao, E. Chason, and S. T. Picraux, Phys. Rev. Lett. **67**, 124 (1991)
[34] M. A. Makeev and A.-L. Barabási, Appl. Phys. Lett. **71**, 2800 (1997).